Available online at www.sciencedirect.com
SCIENCE DIRECT®
Journal of Solid State Chemistry 177 (2004) 4058–4066
JOURNAL OF SOLID STATE CHEMISTRY
www.elsevier.com/locate/jssc

Structural and magnetic characterization of Mn_3IrGe and $Mn_3Ir(Si_{1-x}Ge_x)$: experiments and theory

T. Eriksson[a,*], L. Bergqvist[b], P. Nordblad[c], O. Eriksson[b], Y. Andersson[a]

[a] *Department of Materials Chemistry, Uppsala University, Box 538, SE-751 21 Uppsala, Sweden*
[b] *Department of Physics, Uppsala University, Box 530, SE-751 21 Uppsala, Sweden*
[c] *Department of Materials Science, Uppsala University, Box 534, SE-751 21 Uppsala, Sweden*

Received 23 April 2004; received in revised form 23 June 2004; accepted 6 July 2004
Available online 7 October 2004

Abstract

The structural and magnetic properties of a new ternary Ir–Mn–Ge phase, Mn_3IrGe, as well as the solid solution $Mn_3Ir(Si_{1-x}Ge_x)$, $0 \leqslant x \leqslant 1$, have been investigated by means of X-ray and neutron powder diffraction, magnetization measurements and first principles calculations. The crystal structure is cubic, of the $AlAu_4$-type (an ordered form of the β-Mn structure), $Z = 4$, space group $P2_13$, and the unit-cell dimension varies linearly with the silicon content. For all compositions, antiferromagnetic ordering is found below a critical temperature of about 225 K. The magnetic structure is noncollinear, as a result of frustrated magnetic interactions on a triangular network of Mn atoms, on which the moments rotate 120° around the triangle axes. The magnitude of the magnetic moment at 10 K is 3.39(4) μ_B for Mn_3IrGe. The theoretical calculations reproduce with very good accuracy the magnitudes as well as the directions of the experimentally observed magnetic moments.

Keywords: Manganese–iridium germanide; Manganese–iridium silicide; Neutron diffraction; Rietveld method; Magnetic structure; Crystal structure; First principles calculations; Susceptibility measurements; Magnetic frustration

1. Introduction

The magnetic interactions in manganese-based systems are of general interest, since among the transition metals, Mn-based compounds are almost exclusively the ones that may form noncollinear, complex magnetic structures [1]. One may speculate about reasons for this, such as complex RKKY interactions [2,3], frustrated antiferromagnetic interactions, or band structure effects [4]. Recently, noncollinear, antiferromagnetic order was reported for the new phase Mn_3IrSi [5]. The reason for the noncollinear ordering was suggested to be strong antiferromagnetic couplings that are frustrated by a triangular geometry of the magnetic interactions between the nearest-neighbor manganese atoms [5].

The magnetic properties of Mn_3IrSi are of particular interest, since the compound crystallizes in the $AlAu_4$-type structure, a structure similar to β-Mn, a polymorph of manganese that does not order magnetically. The Mn atoms in Mn_3IrSi are in the same 12-fold site as the 12*b* site in β-Mn, whereas the Ir and Si sites are derived from the 8*c* site in β-Mn [5]. It is not quite clear why the replacement of some of the Mn atoms in β-Mn with nonmagnetic elements, such as Ir and Si, leads to magnetic order.

The magnetic properties of β-Mn [6] and its alloys with, for example, Al [6–8], Sn [9,10], and Ru [11] have been discussed recently. It was found that although β-Mn does not order magnetically down to 1.4 K, there is evidence for strong spin fluctuations with antiferromagnetic Mn–Mn interactions. From these works it was suggested that β-Mn is in a spin-liquid state [12–14] that transforms to a spin-glass-like state with increased alloying concentration.

*Corresponding author. Fax: +46-18-51-35-48.
E-mail address: therese.eriksson@mkem.uu.se (T. Eriksson).

0022-4596/$ - see front matter © 2004 Elsevier Inc. All rights reserved.
doi:10.1016/j.jssc.2004.07.001

Since the ternary Ir–Mn–Ge system has not previously been studied, it is of interest to investigate if an analogous phase to Mn_3IrSi, i.e., Mn_3IrGe, exists, and if it exhibits magnetic ordering. This article reports on the preparation and characterization of Mn_3IrGe, as well as the solid solution $Mn_3Ir(Si_{1-x}Ge_x)$, $0 \leqslant x \leqslant 1$. The crystal and magnetic structures are determined by neutron powder diffraction, in combination with magnetization measurements. The experimental results are complemented by theoretical electronic structure, total energy calculations.

2. Experiments and theory

2.1. Sample preparation and phase analysis

Master samples of compositions Mn_3IrGe and Mn_3IrSi, as well as a larger batch of Mn_3IrGe for neutron diffraction measurements, were prepared by melting stoichiometric amounts of the elements in an alumina crucible in a high-frequency vacuum induction furnace under 300 mbar argon atmosphere, by the drop-synthesis method [15]. Starting materials were single crystal pieces of germanium (Highways International, purity 6 N) or silicon (Highways International, purity 99.999%), pressed pellets of iridium powder (Cerac, purity 99.9%), and pieces of manganese metal (Cerac, claimed purity 99.99%, purified from manganese oxides by sublimation). Compounds of $Mn_3Ir(Si_{1-x}Ge_x)$ with $x = 0.10$, 0.30, 0.50, and 0.75 were prepared by melting appropriate amounts of the master samples in an arc furnace under 300 mbar argon atmosphere. All samples were crushed, pressed into pellets, and annealed in evacuated fused silica tubes at 900 °C for 2–4 days and 800 °C for 1–2 weeks and then quenched. The batch of Mn_3IrGe investigated by neutron diffraction techniques was stress relieved at 800 °C for 30 min.

Phase analysis and determination of unit-cell parameters were performed by recording X-ray powder diffraction films with a Guinier–Hägg focusing camera using Cu$K\alpha_1$ radiation, with silicon powder added as internal standard for calibration ($a = 5.43088(4)$ Å at 25 °C).

2.2. Neutron powder diffraction

Neutron powder diffraction data were collected for the Mn_3IrGe sample at the R2 research reactor at NFL in Studsvik, Sweden. The sample was contained in a vanadium cylinder and measurements were performed in the 2θ-range 4–140° in steps of 0.08° at temperatures 295, 170, 110, 60, and 10 K. The neutron beam was monochromated to 1.471 Å using a parallel double Cu (220) monochromator system. An absorption correction was applied using $\mu R = 0.505$, as calculated from a transmission measurement at $2\theta = 0°$.

Structure refinements were performed by the Rietveld method, using the program FULLPROF [16] with the scattering lengths Mn: −3.73 fm; Ir: 10.60 fm; and Ge: 8.185 fm. The pseudo-Voigt function was used to describe the peak shape and the background was modeled by interpolation between fixed points.

For the 295 K data set, 16 parameters were varied. *Profile parameters*: 2θ zero point (1), scale factor (1), profile shape parameter (1), half-width parameters (3), and asymmetry parameters (2); *structural parameters*: atomic coordinates (5), lattice parameter (1), and isotropic temperature factors (2).

For the 170, 110, 60, and 10 K data sets, the *x*-, *y*-, and *z*-components of a magnetic moment localized on the manganese atoms were varied, as well as the profile and structural parameters listed above (with the exception that an overall isotropic temperature factor was used), resulting in 18 varied parameters. The nuclear and magnetic contributions to the diffraction intensities were treated as two separate phases, with the magnetic phase described in space group *P*1, using the magnetic form factor coefficient of Mn(0).

2.3. Magnetization measurements

Measurements of magnetization versus temperature were performed for all samples, using a SQUID magnetometer in the temperature range 10–300 K with an applied field of 250 Oe. Field-dependent magnetization measurements were performed for the Mn_3IrGe sample (neutron diffraction batch) at 120 K in the range −10 to 10 kOe.

2.4. Details of calculations

The electronic structure and total energy calculations for Mn_3IrGe and Mn_3IrSi were based on density functional theory [17,18] in the local spin density approximation [19]. A scalar-relativistic tight-binding linear-muffin–tin orbital method in the atomic sphere approximation (TB-LMTO-ASA) [20,21] was employed. Optimization of the muffin–tin spheres radii were performed to minimize the sphere overlap. The program can handle noncollinear magnetic structures and its implementation [22] follows the scheme presented in Ref. [23]. Within each muffin–tin sphere, a unique spin quantization axis is constructed, which is different for different spheres. In this way, only noncollinearity on an inter-atomic level is treated, while noncollinearity inside the muffin–tin spheres [24] is neglected. Each magnetic moment inside the muffin–tin sphere *i* in the crystal is

then described by assigning Cartesian coordinates:

$$\bar{M}_i = M(\sin\theta_i \cos\phi_i, \sin\theta_i \sin\phi_i, \cos\theta_i) = (M_{xi}, M_{yi}, M_{zi}), \quad (1)$$

where θ_i and ϕ_i are the Euler angles and M the magnitude of the magnetic moment $\bar{M}_i$.

The magnetic moments were allowed to relax to the ground state configuration by calculating the magnetic forces on each magnetic moment. In these calculations, no symmetry constraints were imposed on the magnetic structure. The calculations are carefully converged with respect to both the number of k-points in the Brillouin zone (343 k-points in the full BZ-zone were used), the size of the basis set ($l_{max} = 2$ was used, $l_{max} = 3$ was tested and gave essentially the same result as $l_{max} = 2$), and the self-consistency criterion. The Brillouin zone integration used a broadening technique [25] where each eigenvalue is smeared with a width of 12.7 mRy in order to speed up convergence. In all calculations the atomic positions and lattice constant determined experimentally at room temperature were used, and no atomic relaxation was allowed.

3. Results and discussion

3.1. Crystal structure

Mn_3IrGe was found to crystallize in the $AlAu_4$-type structure [26], an ordered form of the β-Mn structure type [27,28], with the space group $P2_13$. Germanium occupies a 4*a* site, iridium a second 4*a* site and manganese the 12*b* site. This corresponds to four formula units of Mn_3IrGe per unit cell. The structural parameters, obtained from refinements by the Rietveld method, are listed in Table 1 for neutron diffraction data collected at 295 K, and the observed and calculated diffraction profiles are shown in Fig. 1. Within experimental errors, all sites are fully occupied, with no evidence of mixed occupancy. Inter-atomic distances up

Table 1
Final structural parameters for Mn_3IrGe at 295 K

Atom	Wyckoff position	x	y	z	B_{iso} (Å^2)
Mn	12*b*	0.117(1)	0.199(1)	0.458(1)	0.25(5)
Ir	4*a*	0.6853(6)	0.6853	0.6853	0.17(2)
Ge	4*a*	0.0616(8)	0.0616	0.0616	0.17[a]

$R_p = 4.23\%$; $R_{wp} = 5.73\%$; $R_{exp} = 4.04\%$; $\chi^2 = 2.01$; $R_{Bragg} = 4.04\%$

Estimated standard deviations within parentheses. Space group: $P2_13$ (no. 198); unit-cell parameter: $a = 6.6260(2)$ Å.
[a]Isotropic temperature factors of Ir and Ge were restrained to have the same value.

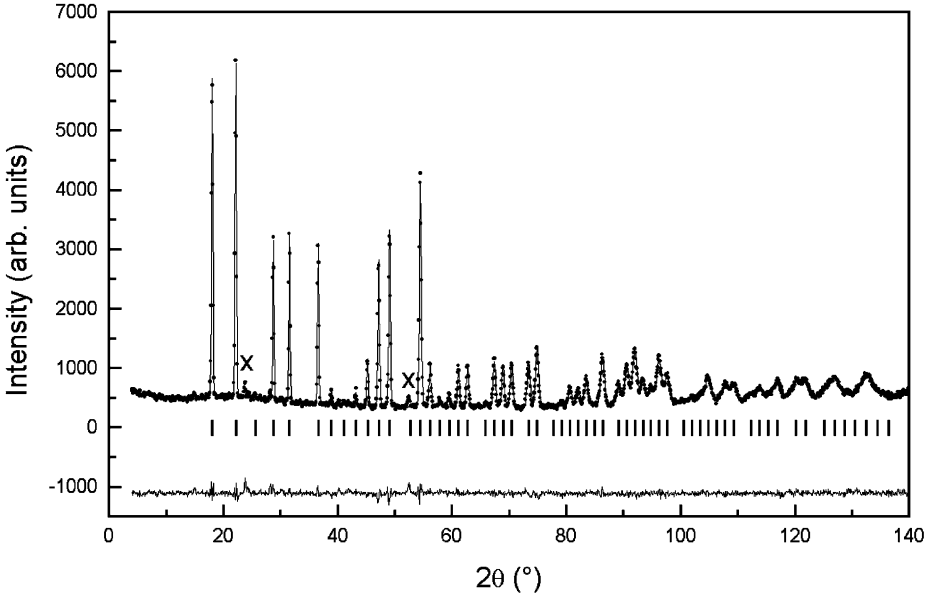

Fig. 1. Observed (points), calculated (solid line), and difference (bottom, solid line) neutron powder diffraction profiles for Mn_3IrGe at 295 K. Tick marks indicate the positions of Bragg reflections. Crosses indicate the two most pronounced peaks from a minor impurity phase.

Table 2
Interatomic distances in Mn_3IrGe at 295 K

Atoms	Distance (Å)	Atoms	Distance (Å)
Mn–Ge	2.68(1)	Ir–3 Ge	2.482(2)
Mn–2 Mn	2.69(2)	Ir–3 Mn	2.70(1)
Mn–Ir	2.70(1)	Ir–3 Mn	2.76(1)
Mn–Ir	2.76(1)	Ir–3 Mn	2.808(9)
Mn–2 Mn	2.78(2)		
Mn–Ir	2.808(9)	Ge–3 Ir	2.482(2)
Mn–Ge	2.81(1)	Ge–3 Mn	2.68(1)
Mn–Ge	2.825(9)	Ge–3 Mn	2.81(1)
Mn–2 Mn	2.89(2)	Ge–3 Mn	2.825(9)
Mn–2 Mn	3.425(4)		

Estimated standard deviations within parentheses.

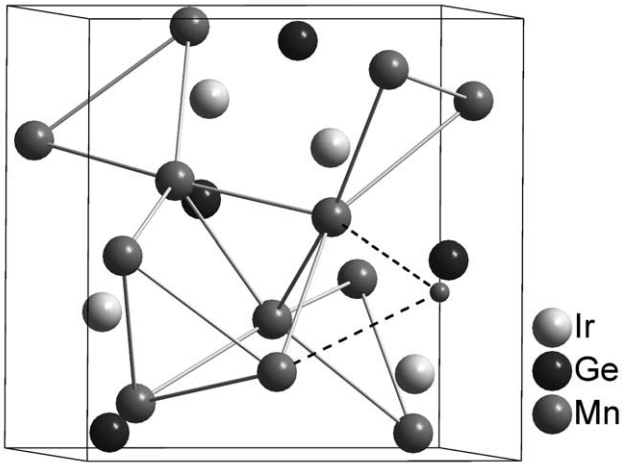

Fig. 2. Crystal structure of Mn_3IrGe. Links are drawn between near neighbor Mn atoms, forming a network of corner sharing triangles. One Mn atom outside the unit cell (smaller, with hatched links) is added to illustrate that all corners are shared between three triangles.

to 3.5 Å were calculated and are listed in Table 2. The closest Mn–Mn distances are found on a network of equilateral triangles, with each corner (Mn atom) shared between three triangles with slightly different side lengths, as illustrated in a drawing of the unit cell in Fig. 2. Mn_3IrGe is isostructural with the recently reported phase Mn_3IrSi [5].

3.2. Phase analysis

X-ray powder diffraction films recorded for the substitution series $Mn_3Ir(Si_{1-x}Ge_x)$ with $x = 0.00$, 0.10, 0.30, 0.50, 0.75, and 1.0 demonstrate a complete range of solid solubility between Mn_3IrSi and Mn_3IrGe, with a linear concentration dependence of the lattice parameter, see Table 3. Diffraction films recorded for $x = 0.00$, 0.10, and 0.30 display a few weak additional lines from the impurity phase IrMnSi, whereas samples with $x = 0.50$, 0.75, and 1.0 are single phase. The larger batch of Mn_3IrGe, used for neutron diffraction investigations, contains some very small amounts of an extra phase that could not be identified. The reflections from this phase, marked with crosses in the 295 K neutron powder diffractogram in Fig. 1, do not significantly change intensities at lower temperatures.

Table 3
Lattice parameters for the solid solution $Mn_3Ir(Si_{1-x}Ge_x)$ at 295 K

Composition	Lattice parameter (Å)
Mn_3IrSi	6.4988(1)
$Mn_3IrSi_{0.90}Ge_{0.10}$	6.5156(2)
$Mn_3IrSi_{0.70}Ge_{0.30}$	6.5382(2)
$Mn_3IrSi_{0.50}Ge_{0.50}$	6.5653(2)
$Mn_3IrSi_{0.25}Ge_{0.75}$	6.5956(2)
Mn_3IrGe	6.6260(2)

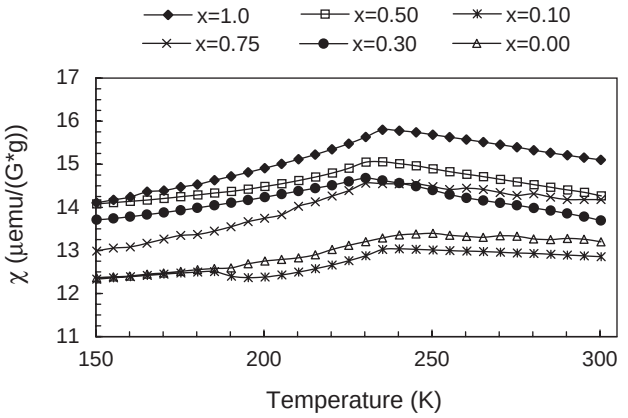

Fig. 3. Magnetic susceptibility (χ) versus temperature for the substitution series $Mn_3Ir(Si_{1-x}Ge_x)$ ($x = 1.0$, 0.75, 0.50, 0.30, 0.10, and 0.00).

3.3. Magnetic properties

The magnetic response (field and temperature dependence) of Mn_3IrGe and $Mn_3Ir(Si_{1-x}Ge_x)$ show a very similar behavior to that of Mn_3IrSi [5]. The magnetization (M) versus magnetic field (H) curves are closely linear in field. The derived magnetic susceptibility ($\chi = M/H$) always stays at about 1.3×10^{-5} emu/(G g) and is weakly temperature dependent. The temperature dependence of the susceptibility (measured in a field of 250 Oe, using a zero field cooled (ZFC) procedure) for all samples in the $Mn_3Ir(Si_{1-x}Ge_x)$ series is plotted in Fig. 3. The most significant feature of the different ZFC susceptibility curves is that they all show a broad maximum at 230–240 K indicating an antiferromagnetic transition. The transition temperature, as defined from the maximum in $d(\chi T)/dT$, is found at 225 ± 10 K for all samples. The magnitude of the susceptibility varies only slightly between the different samples and does not show a regular trend with the concentration of Ge.

Another property that all samples have in common is illustrated in Fig. 4 by ZFC and field cooled (FC) magnetization curves, $M(T)$, for the $Mn_3Ir(Si_{0.50}Ge_{0.50})$ sample (measured with $H = 250$ Oe). There appears an excess magnetization at temperatures below T_N, i.e., a difference between the ZFC and the FC magnetization. This excess magnetization can be assigned to some uncompensated magnetic moments in the bulk of the material, due to defects, or in antiferromagnetic domain walls. In addition, as is also illustrated in Fig. 4, there is a sudden increase of the FC magnetization at low temperatures ($T < 100$ K). This enhancement is accompanied by only a small bump in the ZFC magnetization. A corresponding behavior also occurs in the other samples, but the very onset temperature and magnitude of the enhancement is different for the different samples. This feature indicates that the complex antiferromagnetic ordering that occurs in this frustrated system is quite subtle, and that imbalance can appear in the interaction pattern with decreasing temperature, causing parts of the spins to deviate from their ideal directions and giving rise to local net magnetic moments. These moments can align with the field in an FC process, whereas they become locked in random directions in a ZFC process and are only revealed as a weak bump in the ZFC $M(T)$ curve.

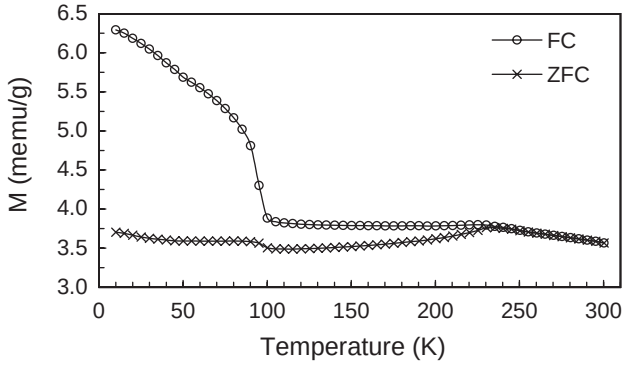

Fig. 4. Temperature dependence of the FC and ZFC magnetization (M) for $Mn_3Ir(Si_{0.50}Ge_{0.50})$.

3.4. Experimental magnetic structure

The neutron powder diffraction patterns recorded below the magnetic transition temperature show magnetic contributions to the observed intensities. The magnetic contributions are well explained by a noncollinear antiferromagnetic structure, as can be seen in Fig. 5, which shows the observed and calculated diffraction profiles at 10 K. The refined structural parameters and total magnetic moment on Mn at 10 K are listed in Table 4. The magnetic moment on Mn in Mn_3IrGe, obtained from structure refinements for the 10 K data set, is $3.39(4)\,\mu_B$. No significant differences from the values listed in Table 4 were obtained in the refinements of the 60 and 110 K data sets, whereas the magnitude of the magnetic moment decreased slightly ($3.07(4)\,\mu_B$) for the 170 K data set.

The magnetic moment on, e.g., the Mn atom with position coordinate (0.117, 0.198, and 0.458) has at 10 K the vector components $M_x = 1.4(1)\,\mu_B$, $M_y = 2.4(2)\,\mu_B$, and $M_z = -2.0(2)\,\mu_B$. The directions of the magnetic moments on all 12 Mn atoms can be generated from this vector by rotations around the 3- and 2-fold axes of the crystal structure. The magnetic moments on the network

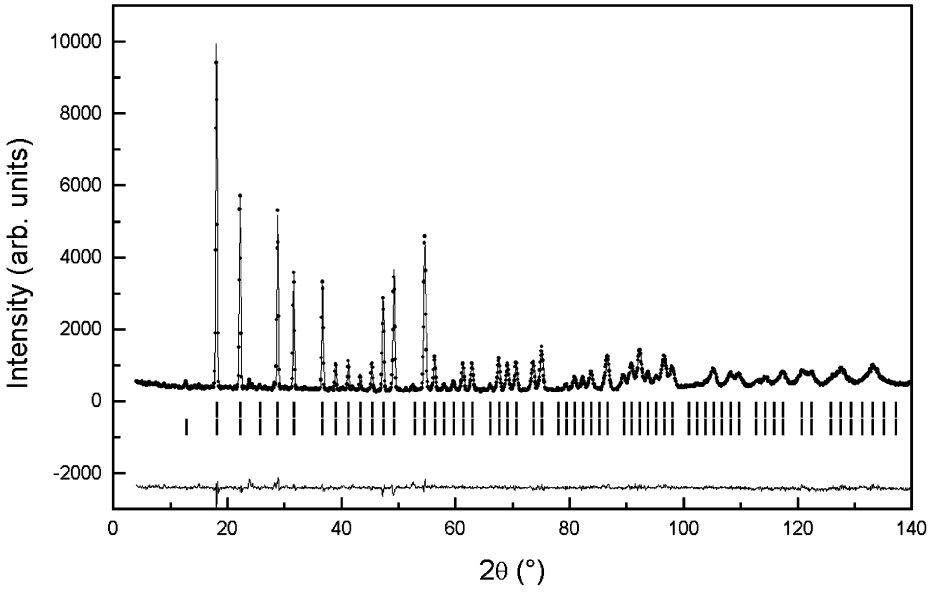

Fig. 5. Observed (points), calculated (solid line), and difference (bottom, solid line) neutron powder diffraction profiles for Mn_3IrGe at 10 K. Upper tick marks indicate the positions of Bragg reflections for the crystal structure and lower tick marks for the magnetic structure.

Table 4
Final structural parameters and magnetic moment for Mn_3IrGe at 10 K

Atom	Wyckoff position	x	y	z	$M(\mu_B)$
Mn	12*b*	0.117(1)	0.198(1)	0.458(1)	3.39(4)
Ir	4*a*	0.6870(7)	0.6870	0.6870	
Ge	4*a*	0.0640(9)	0.0640	0.0640	

$B_{overall} = 0.01(2)\,\text{Å}^2$

$R_p = 4.74\%$; $R_{wp} = 6.44\%$; $R_{exp} = 4.10\%$; $\chi^2 = 2.46$; $R_{Bragg} = 5.54\%$; $R_{mag} = 5.55\%$

Estimated standard deviations within parentheses. Unit-cell parameter: $a = 6.6090(2)$ Å.

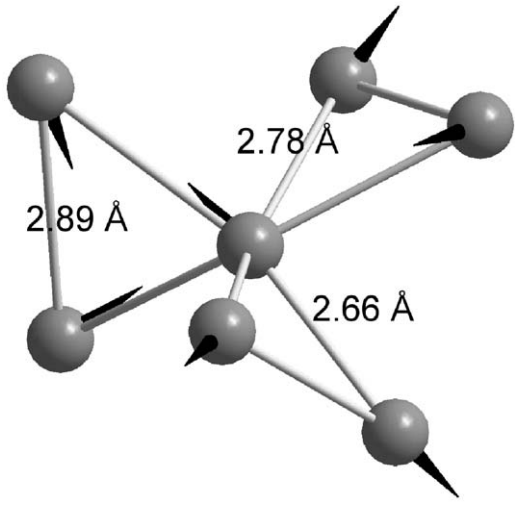

Fig. 6. Orientation of the magnetic moments on three linked triangles of Mn atoms. Mn–Mn distances at 10 K on the respective equilateral triangles are indicated.

of equilateral Mn triangles cancel within a magnetic unit cell of the same size as the crystallographic cell. For each Mn triangle, the projections of the magnetic moments on the triangle plane form 120° angles, as illustrated in Fig. 6. The magnetic structure of Mn_3IrGe was found to be very similar to the previously reported magnetic ordering of Mn_3IrSi [5], for which a more thorough description of the magnetic structure was provided. The Mn magnetic moment at 10 K was reported to be $2.97(4)\,\mu_B$ for Mn_3IrSi, which is somewhat lower than what is observed at the same temperature for Mn_3IrGe. In accord with the argument in Ref. [5], we suggest that the observed noncollinear order in Mn_3IrGe is the result of geometrically frustrated antiferromagnetic interactions.

3.5. Theoretical magnetic structure

Several magnetic configurations of the Mn atoms in Mn_3IrSi and Mn_3IrGe have been considered: ferromagnetic, four different collinear antiferromagnetic, and the experimental noncollinear antiferromagnetic arrangement. The total energies of the different configurations are displayed in Table 5, with the energy of the noncollinear magnetic structure used as a reference level and set to zero. The results for Mn_3IrSi and Mn_3IrGe are very similar and are discussed together. The ferromagnetic configuration corresponds to the highest energy of the considered configurations, by an amount of approximately 16 mRy/Mn atom above the ground state. Much lower in energy lie the four different collinear antiferromagnetic configurations, which are all similar in energy (3–6 mRy/Mn atom for Mn_3IrSi and 4–6 mRy/Mn atom for Mn_3IrGe). The configuration with the lowest energy is the experimentally observed noncollinear antiferromagnetic arrangement of the Mn magnetic moments. In the calculations, we relaxed the magnetic structure to the ground state by calculating the magnetic forces on each atom starting from the magnetic structure suggested by experiments. The values for Mn_3IrSi differ slightly from our previous report [5] due to some minor differences in the set up of the calculations.

Table 5
Total energies in mRy/Mn atom of different magnetic configurations

Configuration	Mn_3IrSi	Mn_3IrGe
Ferromagnetic	15.8	16.0
Collinear antiferromagnetic	2.8–5.8	4.1–6.2
Noncollinear	0	0

Noncollinear magnetic structure is used as reference level and is set to zero.

In Table 6 the calculated and experimental magnetic Mn moments are displayed for the ground state magnetic structure of Mn_3IrSi. The agreement between theory and experiment is remarkably good in this case, both the directions of the magnetic moments and the magnitudes are reproduced (calculated value is $3.0\,\mu_B$/Mn atom, to be compared with the observed value of $2.97(4)\,\mu_B$). The calculations give very small induced moments on Ir ($0.03\,\mu_B$) and Si ($0.01\,\mu_B$). In Table 7, the same results as above are shown for Mn_3IrGe. The directions of the magnetic moments of Mn agree well between theory and experiment, but the magnitudes differ slightly. Theory gives a somewhat smaller Mn magnetic moment of $3.18\,\mu_B$, while experiments give $3.39(4)\,\mu_B$. Very small induced moments (less than $0.02\,\mu_B$) were found on Ir and Ge.

In Fig. 7, the density of states (DOS) for Mn_3IrSi (upper panel) and for Mn_3IrGe (lower panel) are shown. The spin-down states are represented with negative values. The Mn 3*d* states are shown with the thickest line, the Ir 5*d* states are shown with the thinner line, and all states of Si and Ge, respectively, are shown with a

Table 6
Experimental and theoretical magnetic moments of Mn_3IrSi in *x*-, *y*-, and *z*-components, which describe the direction of the magnetic moment on each manganese atom

Atom	Calculated			Experimental		
	M_x	M_y	M_z	M_x	M_y	M_z
Mn 1	1.26	2.29	−1.47	1.3(1)	2.3(1)	−1.4(1)
Mn 2	−1.26	−2.29	−1.47	−1.3(1)	−2.3(1)	−1.4(1)
Mn 3	−1.26	2.29	1.47	−1.3(1)	2.3(1)	1.4(1)
Mn 4	1.27	−2.29	1.47	1.3(1)	−2.3(1)	1.4(1)
Mn 5	−1.48	1.29	2.27	−1.4(1)	1.3(1)	2.3(1)
Mn 6	−1.48	−1.29	−2.27	−1.4(1)	−1.3(1)	−2.3(1)
Mn 7	1.48	−1.29	2.27	1.4(1)	−1.3(1)	2.3(1)
Mn 8	1.48	1.29	−2.27	1.4(1)	1.3(1)	−2.3(1)
Mn 9	2.28	−1.44	1.30	2.3(1)	−1.4(1)	1.3(1)
Mn 10	−2.29	−1.45	−1.30	−2.3(1)	−1.4(1)	−1.3(1)
Mn 11	2.28	1.44	−1.30	2.3(1)	1.4(1)	−1.3(1)
Mn 12	−2.28	1.45	1.30	−2.3(1)	1.4(1)	1.3(1)

Mn atoms are numbered as the equivalent coordinates of the 12*b* site in space group $P2_13$ in the International Tables for Crystallography.

Table 7
Experimental and theoretical magnetic moments of Mn_3IrGe in *x*-, *y*-, and *z*-components, which describe the direction of the magnetic moment on each manganese atom

Atom	Calculated			Experimental		
	M_x	M_y	M_z	M_x	M_y	M_z
Mn 1	1.33	2.24	−1.83	1.4(1)	2.4(2)	−2.0(2)
Mn 2	−1.33	−2.23	−1.83	−1.4(1)	−2.4(2)	−2.0(2)
Mn 3	−1.33	2.24	1.83	−1.4(1)	2.4(2)	2.0(2)
Mn 4	1.33	−2.23	1.83	1.4(1)	−2.4(2)	2.0(2)
Mn 5	−1.85	1.33	2.22	−2.0(2)	1.4(1)	2.4(2)
Mn 6	−1.85	−1.33	−2.22	−2.0(2)	−1.4(1)	−2.4(2)
Mn 7	1.85	−1.33	2.22	2.0(2)	−1.4(1)	2.4(2)
Mn 8	1.85	1.33	−2.22	2.0(2)	1.4(1)	−2.4(2)
Mn 9	2.22	−1.83	1.36	2.4(2)	−2.0(2)	1.4(1)
Mn 10	−2.22	−1.83	−1.36	−2.4(2)	−2.0(2)	−1.4(1)
Mn 11	2.22	1.83	−1.36	2.4(2)	2.0(2)	−1.4(1)
Mn 12	−2.22	1.83	1.36	−2.4(2)	2.0(2)	1.4(1)

Mn atoms are numbered as the equivalent coordinates of the 12*b* site in space group $P2_13$ in the International Tables for Crystallography.

dashed line. The DOS for Mn_3IrSi and Mn_3IrGe are very similar and have the same kind of features. The Mn 3*d* states show a large spin-splitting consistent with the large magnetic moment on Mn and the Mn spin-up band is saturated. The Ir and Si (Ge) states show practically no exchange splitting. In the energy interval −0.5 to −0.2 mRy with respect to the Fermi level, some hybridization between the Mn and Ir states can be noted, since the DOS features of the Mn and Ir states are correlated and follow each other.

4. Conclusions

A new ternary Ir–Mn–Ge phase, of stoichiometry Mn_3IrGe, has been synthesized. It crystallizes in the $AlAu_4$-type structure, an ordered form of the β-Mn structure. Mn_3IrGe is isostructural to the previously reported phase Mn_3IrSi, and a complete range of solid solubility was demonstrated. The magnetic structure of Mn_3IrGe is noncollinear antiferromagnetic, closely similar to that of Mn_3IrSi. The Mn atoms form a triangular network, on which the moments are rotated 120° around the triangle axes. This is the result of strong antiferromagnetic interactions, frustrated by the triangular geometry. The magnetic moment on Mn is $3.39(4)\,\mu_B$ at 10 K for Mn_3IrGe, which is higher than the value of $2.97(4)\,\mu_B$ previously observed for Mn_3IrSi. The magnetization curves of all samples in the $Mn_3Ir(Si_{1-x}Ge_x)$ series show similar characteristics, with a Néel temperature (T_N) of 225 ± 10 K for all compositions. It is interesting that the magnetic moment

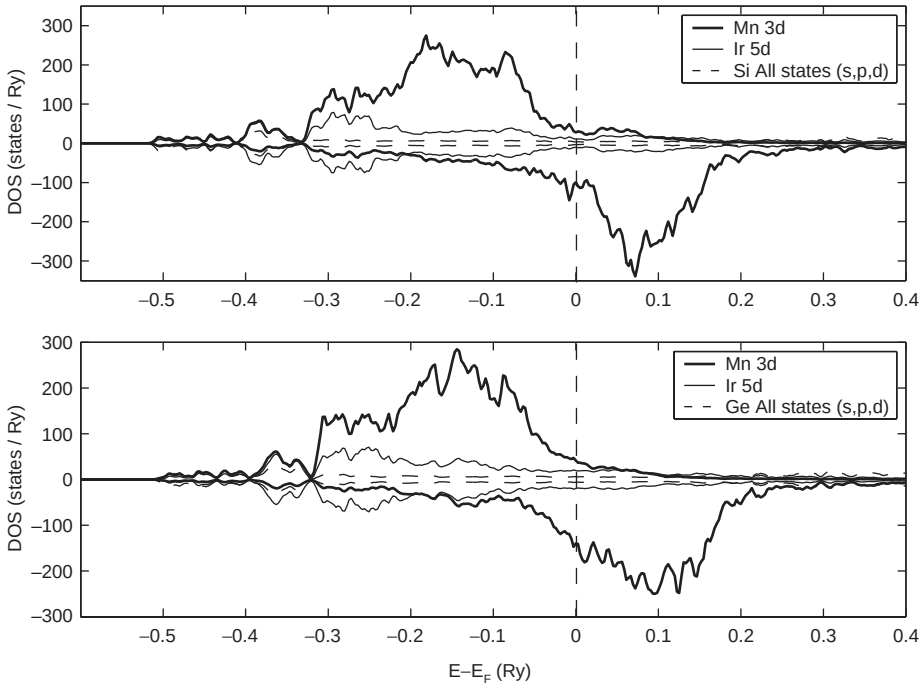

Fig. 7. DOS of Mn_3IrSi (upper panel) and Mn_3IrGe (lower panel). The energies are given relative to the Fermi level, which is indicated by a vertical dashed line.

increases without any accompanying changes of the Néel temperature. This could be explained by suppression of the critical temperature, caused by frustration of strong antiferromagnetic couplings. Similar observations have been made, for example, in the jarosites [29], with frustrated antiferromagnetic interactions on a Kagome lattice. In $NaFe_3(SO_4)_2(OH)_6$, substitution of Na^+ for K^+ or NH_4^+ leads to only very small changes of the critical temperature [29]. First principles calculations have been shown to reproduce the experimental magnetic structures of Mn_3IrSi and Mn_3IrGe, both concerning the magnitudes and the directions of the magnetic moments. The fact that the magnetic structures of Mn_3IrGe and Mn_3IrSi are very similar, suggests a common nature of the exchange interactions, based on delocalized electron states, in these two compounds.

Acknowledgments

We would like to thank Martin Sahlberg for participation in sample preparations. Håkan Rundlöf is acknowledged for skilful assistance in neutron powder diffraction data collection. Financial support from the Swedish Research Council (VR) and the Swedish Foundation for Strategic Research (SSF) is acknowledged. O.E. is grateful to the Göran Gustafsson foundation, and to the Centre for Dynamical Processes, Uppsala University, for support.

References

[1] J. Kübler, Theory of Itinerant Electron Magnetism, Oxford Science Publications, Oxford, 2000.
[2] R.J. Elliot, F.A. Wedgwood, Proc. Phys. Soc. 81 (1963) 846–855.
[3] J. Jensen, A.R. Mackintosh, Rare Earth magnetism, Clarendon Press, Oxford, 1991.
[4] R. Lizárraga et al., unpublished.
[5] T. Eriksson, R. Lizárraga, S. Felton, et al., Phys. Rev. B 69 (2004) 054422.
[6] H. Nakamura, K. Yoshimoto, M. Shiga, M. Nishi, K. Kakurai, J. Phys.: Condens. Matter 9 (1997) 4701–4728.
[7] J.R. Stewart, R. Cywinski, Phys. Rev. B 59 (1999) 4305–4313.
[8] J.R. Stewart, R. Cywinski, J. Magn. Magn. Mater. 272–276 (2004) 676–678.
[9] J.B. Dunlop, J.M. Williams, J. Crangle, Physica 86–88B (1977) 269–271.
[10] Y. Nakai, J. Phys. Soc. Jpn. 63 (1994) 775–780.
[11] K. Sasao, R.Y. Umetsu, K. Fukamichi, J. Alloys Compds. 325 (2001) 24–28.
[12] S.H. Lee, C. Broholm, G. Aeppli, T.G. Perring, B. Hessen, A. Taylor, Phys. Rev. Lett. 76 (1996) 4424–4427.
[13] P. Schiffer, A.P. Ramirez, D.A. Huse, A.J. Valentino, Phys. Rev. Lett. 73 (1994) 2500–2503.
[14] O.A. Petrenko, C. Ritter, M. Yethiraj, D. McK Paul, Phys. Rev. Lett. 80 (1998) 4570–4573.
[15] S. Rundqvist, Chem. Scr. 28 (1988) 15–20.
[16] J. Rodríguez-Carvajal, FULLPROF computer program, version 2.45, LLB, Saclay, 2003.
[17] P. Hohenberg, W. Kohn, Phys. Rev. 136 (1964) B864–B871.
[18] W. Kohn, L.J. Sham, Phys. Rev. 140 (1965) A1133–A1138.
[19] J.P. Perdew, K. Burke, M. Enzerhof, Phys. Rev. Lett. 77 (1996) 3865–3868.
[20] O.K. Andersen, Phys. Rev. B 12 (1975) 3060–3083.

[21] O.K. Andersen, O. Jepsen, Phys. Rev. Lett. 53 (1984) 2571–2574.
[22] The computer code was made in-house, based on the original method published in Ref. [20]. For details, see www.fysik.uu.se/theomag.
[23] L.M. Sandratskii, Adv. Phys. 47 (1998) 91–160.
[24] L. Nordström, D.J. Singh, Phys. Rev. Lett. 76 (1996) 4420–4423.
[25] M. Methfessel, A.T. Paxton, Phys. Rev. B 40 (1989) 3616–3621.
[26] O.E. Ullner, Ark. Kemi Mineral. Geol. 14A (1940) 1–20.
[27] G.D. Preston, Philos. Mag. 5 (1928) 1207–1225.
[28] C.B. Shoemaker, D.P. Shoemaker, T.E. Hopkins, S. Yindepit, Acta Crystallogr. B 34 (1978) 3573–3576.
[29] A.S. Wills, Can. J. Phys. 79 (2001) 1501–1510.